Coastal Engineering 57 (2010) 1–18

Contents lists available at ScienceDirect

Coastal Engineering

journal homepage: www.elsevier.com/locate/coastaleng

Tsunami-like solitary waves impinging and overtopping an impermeable seawall: Experiment and RANS modeling

Shih-Chun Hsiao [a,*], Ting-Chieh Lin [b]

[a] Department of Hydraulic and Ocean Engineering, National Cheng Kung University, Tainan 701, Taiwan
[b] Research Center of Ocean Environment and Technology, National Cheng Kung University, Tainan 701, Taiwan

ARTICLE INFO

Article history:
Received 19 September 2008
Received in revised form 12 June 2009
Accepted 18 August 2009
Available online 6 October 2009

Keywords:
Tsunami
Solitary wave
Experiment
RANS
Seawall
Wave force

ABSTRACT

This study investigates tsunami-like solitary waves impinging and overtopping an impermeable trapezoidal seawall on a 1:20 sloping beach. New laboratory experiments are performed for describing three typical cases: a turbulent bore rushes inland and subsequently impacts and overtops the seawall (Type 1); a wave directly collapses on the seawall and then generates overtopping flow (Type 2); and, a wave straightforwardly overtops the seawall crown and collapses behind the seawall (Type 3). A two-dimensional volume of fluid (VOF) type model called the COBRAS (COrnell BReaking And Structure) model, which is based on the Reynolds-Averaged Navier–Stokes (RANS) equations and the k–ε turbulence closure solver, is validated by experimental data and then applied to investigate wave dynamics for which laboratory data are unavailable. Additionally, a set of numerical experiments is conducted to examine the dynamic wave acting force due to waves impacting the seawall. Effects of wave nonlinearity and freeboard are elucidated. Special attention is given to a distinct vortex evolutionary behavior behind the seawall, in which the dynamic properties of entrapped air-bubbles are briefly addressed experimentally and numerically.

1. Introduction

Tsunami-wave trains, which eventually break near the shoreline, may form a sequence of turbulent bores propagating toward shallow water or alternatively collapse upon nearshore breakwaters, thereby generating overtopping flow. Such violent breaking waves and their accompanying wave forces can cause different structure failure mechanisms [see Fig. 2 in Kato et al. (2005)], in which the generated turbulence and vorticity also contribute to large-scale sediment transportation and scouring near the toe of a coastal breakwater, thereby creating structure instability (e.g. Tonkin et al., 2003; Nakamura et al., 2008). This study is therefore of crucial importance for tsunami hazard mitigation and coastal hydrodynamics.

Due to simulation simplicity and similarity of wave hydrodynamics, solitary-type long waves have been employed for decades to study tsunami behavior (Liu et al., 1991; Synolakis and Bernard, 2006). Particularly, solitary waves interacting with coastal objects have garnered considerable attention in terms of wave run-up on a uniform slope (e.g. Lin et al., 1999; Carrier et al., 2003; Li and Raichlen, 2003; Hsiao et al., 2008; Chang et al., 2009), disintegration and transmission properties of waves over an abrupt topography (e.g. Losada et al., 1989; Liu and Cheng, 2001; Lin, 2004), wave–structure interaction between a wave/bore and a vertical/floating barrier (e.g. Ramsden, 1996; Liu and Al-banaa, 2004; Xiao and Huang, 2008), vortex shedding and advection around a submerged obstacle or a sub-aerial plate (e.g. Chang et al., 2001; Lin et al., 2005) and free surface kinematics of a wave passing through a porous structure (e.g. Lynett et al., 2001). However, only a few studies have examined of a solitary wave with overtopping flow impinging upon a coastal structure. Dodd (1998) indicated that his simulated free surface based on a shallow water-wave model did not agree with experimental findings, and pressure data were not reported. Stansby (2003), who devoted to a development of Boussinesq model, did not experimentally calibrate computational results. Kato et al. (2005) examined the behaviors of waves impinging on a seawall, but did not account for the corresponding free surface measurements. Notably, this absence of laboratory information can lead to an inaccurate model (Grilli et al., 1994). One purpose of this study is to conduct an integrated experiment to bridge the gap between solitary waves impinging and overtopping information noted in these studies.

The processes combining both wave impinging and overtopping have complex wave hydrodynamics. Although laboratory experiments can provide insights into a real flow-field environment, such works are costly, time-consuming and can generate unanticipated factors in some circumstances (Hughes, 1993). For instance, Chen and Melville (1988) stated that "However, at each wall location, identical incident wave conditions could yield significantly different impact pressures, mainly because of the randomness of the entrapped-air dynamics during wave breaking." The correlation between pressure data and entrapped air-bubbles is also discussed in this study.

* Corresponding author. Tel.: +866 2757575x63262; fax: +886 6 2741463.
E-mail address: schsiao@mail.ncku.edu.tw (S.-C. Hsiao).

0378-3839/$ – see front matter © 2009 Elsevier B.V. All rights reserved.
doi:10.1016/j.coastaleng.2009.08.004

Moreover, with rapid local fluid acceleration and conspicuous discrete free surface during particular wave run-up/overtopping stages, the popular depth-integrated models can result in incorrect interpretation and simulation breakdown (e.g. Kobayashi and Raichle, 1994; Dodd, 1998; Hu et al., 2000). Fortunately, various sophisticated numerical models due to recent advancements in computer technology have become powerful and efficient tools for exploring complicated wave–structure interaction problems (e.g. Losada et al., 2008). Among these models, the two-dimensional volume of fluid (VOF) type numerical model, called the COrnell BReaking And Structure (COBRAS) model, uses the Reynolds-Averaged Navier–Stokes (RANS) equations to describe mean flow fields, and the modified k–ε closure model is employed to examine turbulence behaviors. This model was successfully developed by Lin and Liu (1998a,b) to simulate surf-zone hydrodynamics of cnoidal waves on a uniform beach. The COBRAS model or the modified version, which is called COBRAS-UC (Losada et al., 2008), has been intensively and successfully validated by numerous coastal experiments (e.g. Garcia et al., 2004; Lara et al., 2006a,b; Lin and Karunarathna, 2007; Torres-Freyermuth et al., 2007; Lara et al., 2008; Losada et al., 2008; Yim et al., 2008; Zhang and Liu, 2008; Guanche et al., 2009). Another goal of this study is to validate the applicability of the COBRAS model to a solitary wave impinging and overtopping a coastal structure, which is unavailable in the previous reports.

This study investigates tsunami-like solitary waves impinging and overtopping an impermeable seawall on a 1:20 sloping beach. Both laboratory experiments and COBRAS modeling are employed. The remainder of this paper is organized as follows. In Section 2, experimental and numerical methods are described. Section 3 compares measurement data and modeling results. Interesting wave dynamics are observed numerically. Section 4 presents a set of numerical experiments for investigating the dynamic wave acting force. Effects of wave nonlinearity and freeboard are discussed. Distinct fluid vorticity with entrapped air-bubbles generated by an overtopping flow behind the seawall is briefly addressed experimentally and numerically. The principal findings are drawn in Section 5.

2. Experimental and numerical methods

This section describes the experimental and numerical methods. Fig. 1(a) presents the layout of present experimental/numerical wave flumes and the symbols for the corresponding physical variables used in analyses. In this study, x and z are the spatial abscissa and ordinate of the Cartesian coordinate system, respectively; H_o is the offshore wave height; η is the local free surface elevation; h_o is the offshore water depth; h is the local water depth; R_c is the freeboard, which is defined as a vertical distance from the still water level to the seawall crown; $\varepsilon = H_o/h_o$ is the wave nonlinearity; t is the physical time; u is the horizontal velocity; v is the vertical velocity; P is the total wave pressure; P_D is the dynamic wave pressure; and F_{DH} and F_{DV} are the horizontal and vertical components of dynamic wave forces, respectively. Notably, "dynamic" means that the response quantities are purely caused by incident waves propagating and then impacting the seawall, i.e. the hydrostatic effect is neglected.

2.1. Experiment

2.1.1. Wave flume setup, measurement apparatus and procedure

The experiments were carried out in a two-dimensional wave flume (22 m long, 0.5 m wide and 0.75 m deep) located in the Tainan

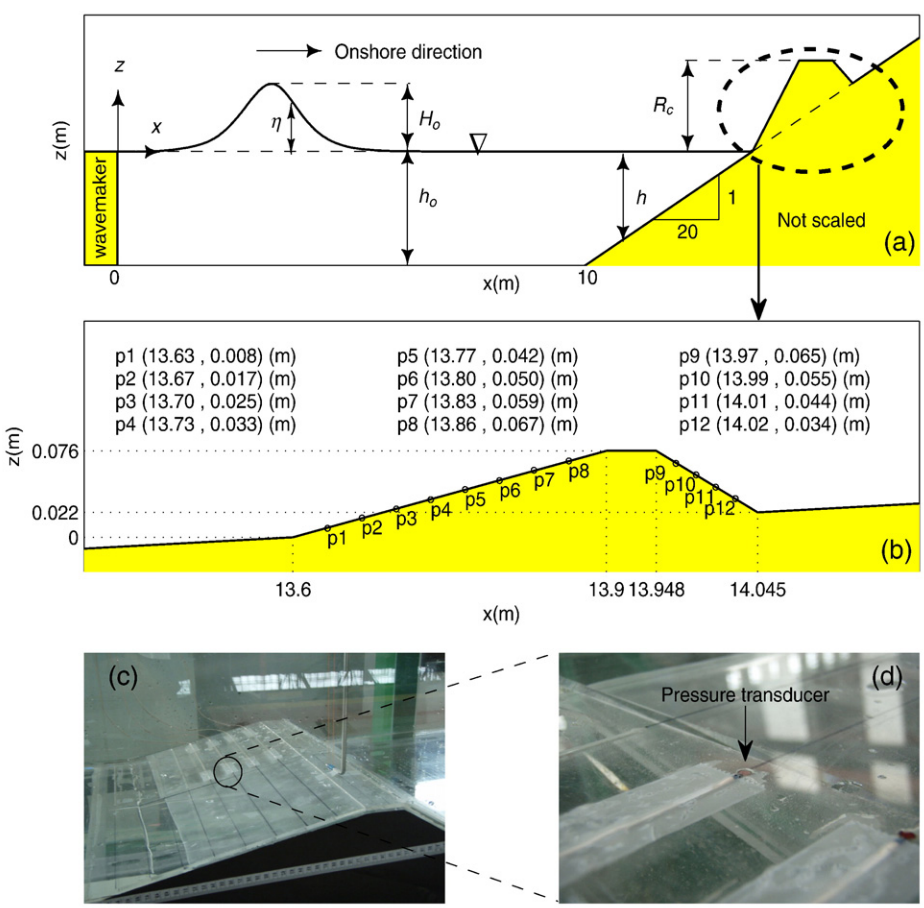

Fig. 1. (a) Sketch of wave flume layout. Symbols are defined for physical variables. (b) Absolute locations of each pressure transducer along the seawall in the coordinate system, i.e. an enclosed ellipse with a black dashed line in subplot (a). (c) A laboratory image of the seawall model. (d) Close-up of the pressure transducer buried in the seawall surface.

Table 1
Experimental conditions of present tsunami cases.

	h_o (m)	H_o (m)	$\varepsilon = \frac{h_o}{H_o}$	R_c (m)
Type 1	0.2	0.07	0.35	0.056
Type 2	0.22	0.0638	0.29	0.036
Type 3	0.256	0.0589	0.23	0

Hydraulics Laboratory (THL), National Cheng Kung University. The flume has glass sidewalls that facilitate recording with a camera and visual observations of the evolutionary processes of waves. Target solitary waves with negligible tail oscillations were generated at one flume end by a programmable piston-type wavemaker using the generation method developed by Goring (1978).

The experimental topography has two sections [Fig. 1(a) and (b)]. One section is a uniform and impermeable aluminum 1:20 slope starting 10 m from the wave paddle (i.e. $x = 10$ m), the slope surface of which is smooth Plexiglas, which significantly reduces friction. The other section is a trapezoidal caisson with seaward 1:4 and landward 1:1.8 slopes, also made of Plexiglas [Fig. 1(b) and (c)]. The seawall model was carefully smoothed and rigidly mounted on the slope starting at a horizontal distance of 3.6 m from the beach toe (i.e. $x = 13.6$ m). Silicone fills with the borders between the seawall, slope and glasswall to prevent fluid infiltration.

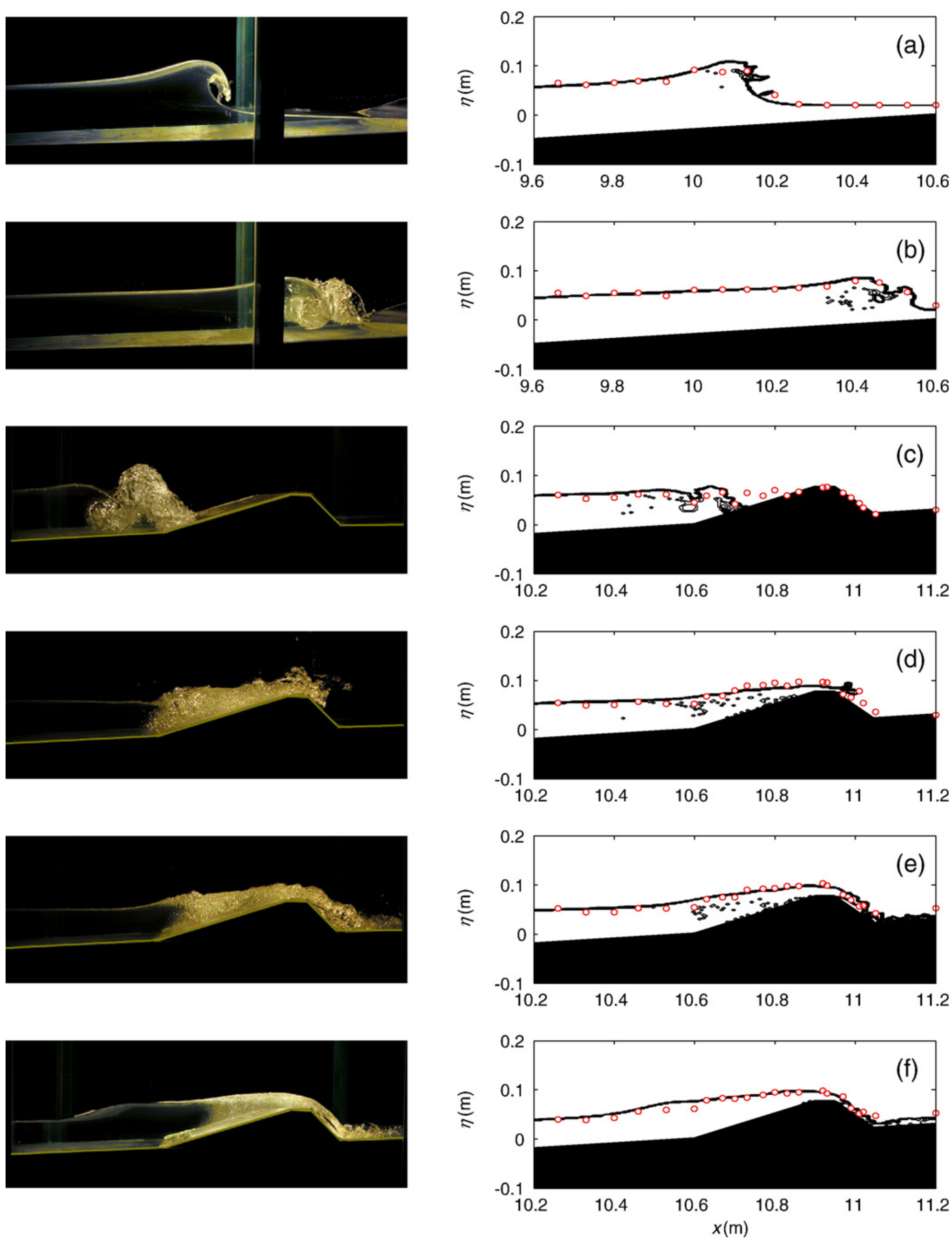

Fig. 2. Qualitative and quantitative comparisons of free surface evolution between laboratory images (left column) and measurement data (right column) (Type 1 wave: $h_o = 0.20$ m, $\varepsilon = 0.35$). Simulated free surface at $t =$ (a) 2.63 s, (b) 2.89 s, (c) 3.01 s, (d) 3.19 s, (e) 3.35 s, (f) 3.71 s; (10 contours of the VOF function with an interval of 0.1 from 0.1 to 1.0 by black solid lines). Experimental data (○).

The local free surface elevation along the flume during experiments was measured using 9 wave gauges. A reference wave gauge was fixed at 1.1 m in front of the beach slope (i.e. $x = 8.9$ m). The dynamic wave impinging load along the seawall surface due to wave interaction was also recorded by 4 tiny pressure transducers, each with a diameter of 3 mm (ST-type by Japan), which were exactly buried in the seawall surface [Fig. 1(c) and (d)]. Pressure was measured at 12 locations along the seawall [see Fig. 1(b)]. The pressure data are utilized to calculate the corresponding wave force acting upon the seawall surface. All gauges were calibrated using a standard method, which concerns the change in water level to adjust the response voltage of each gauge before and after experiments to ensure linearity and stability. The data collection frequencies of the free surface and pressure load were 50 Hz and 1000 Hz, respectively. However, due to the limited number of gauges, identical experiments were reiterated several times and the gauges and transducers were moved to different locations until the full experimental region of interest was covered. The offshore water depth was also measured after each test to maintain the same initial condition. The repeatability of all experiments was satisfactory with a maximum deviation in reference wave height of approximately 3% between repetitions. In total, 54 wave gauges with separated locations in the wave flume and 12 pressure transducers along the seawall surface were utilized. The experimental data were synchronized before analyses. In addition, a high-speed video camera (Nikon COOLPIX5700) with a frame acquisition rate of 3 Hz was also utilized to qualitatively observe the wave profiles during distinct wave evolutionary stages. However, laboratory images and numerical results are not quantitatively compared in this study. The main purpose in obtaining laboratory images is to identify particular wave evolutionary processes qualitatively.

2.1.2. Tsunami-wave cases

Three typical solitary wave cases with different breaking locations were used to simulate approaching tsunami waves. Type 1 comprised a turbulent bore rushing inland and subsequently impacting and overtopping the seawall. Type 2 consisted of a wave directly collapsing on the seawall with overtopping flow subsequently generated. Type 3 was a wave straightforwardly overtopping upon the seawall crown and collapsing behind the seawall. Table 1 summarizes all experimental conditions. These wave types were chosen because they are representative of tsunami waves described in tsunami disaster reports (e.g. Yamamoto et al., 2006; Yeh, 2007). However, although the experiments are highly repeatable, entrapped air-bubbles in wave breaking processes cause unavoidable uncertainties due to the natural complexity of fluid (Chen and Melville, 1988; Kobayashi and Raichle, 1994), as mentioned in Section 1. Such uncertainties would be responsible for some discrepancies in the following experimental and numerical comparisons. Details of comparison are discussed in Section 3.

2.2. COBRAS

The COBRAS model was developed using the two-dimensional RANS equations for the mean flow field and the k–ε equations for the turbulent kinetic energy (TKE), k, and the turbulence dissipation rate,

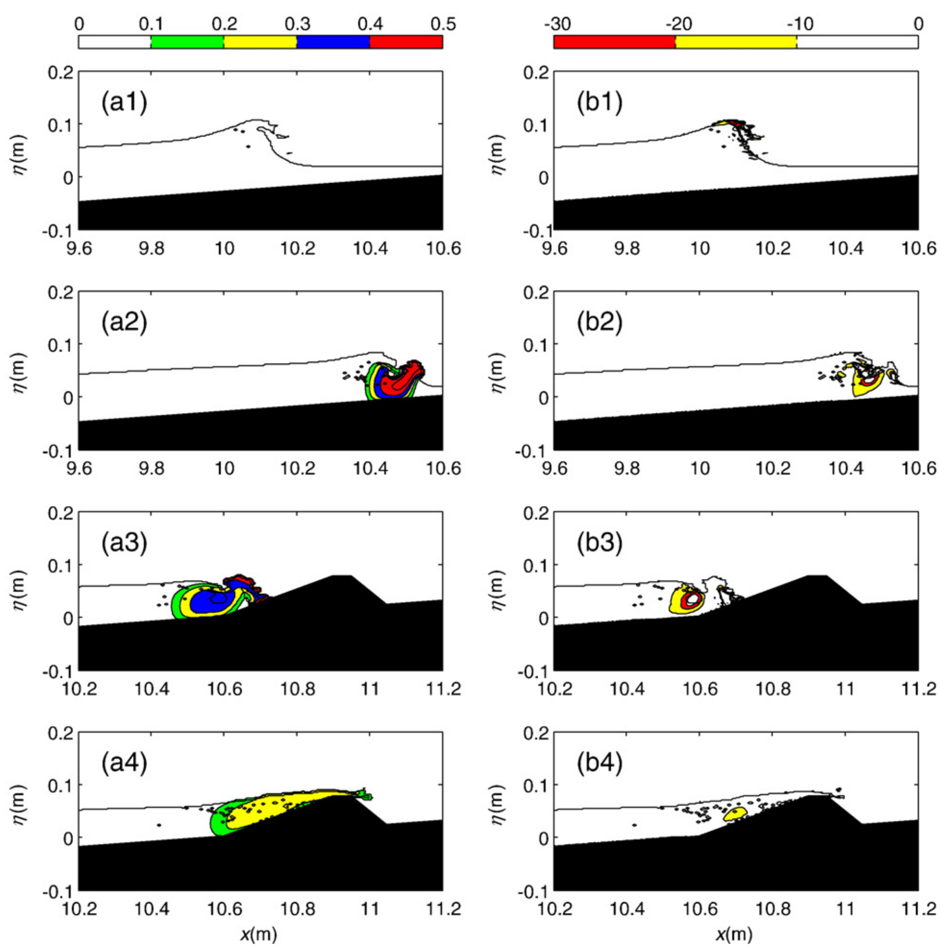

Fig. 3. Simulated (a) turbulent kinetic energy (TKE) (m/s) and (b) vorticity (m^{-1} s) fields for Type 1 wave at $t = 2.89$ s (a1 and b1); 3.01 s (a2 and b2); 3.19 s (a3 and b3); 3.35 s (a4 and b4). Note, only a contour of the VOF function with $\theta = 1.0$ is presented.

ε. The VOF algorithm is applied to track arbitrary free surface deformation. For model details, refer to the studies by Lin (1998) and Lin and Liu (1998a,b). The key issues in simulations are as follows: (1) boundary condition, wave generation and absorption; (2) computational condition; and, (3) solid object treatment and the numerical approaches in simulations.

2.2.1. Boundary condition, wave generation and absorption

In the COBRAS model, a target solitary wave is numerically generated by sending a wave at $x = 0$ m (i.e. left boundary) as an inflow boundary condition. The corresponding free surface η and the velocities u and w are described using the conventional Boussinesq theory (see Lee et al., 1982; Liu and Cheng, 2001; Chang et al., 2001), in which a 99% characteristic length of an infinite solitary wave volume is specified. Note that the left sponge layer for damping unwanted waves was not utilized in this study due to the use of the inflow boundary condition at the left boundary. Therefore the computational time was determined by considering the arrival time when the expected reflected wave caused by seawall touches the left boundary (see Section 2.2.2 for computational conditions). Additionally, the no-slip boundary condition at the solid boundaries is adopted, and the zero-stress condition is applied to the mean free surface for neglecting the air-flow interaction. For the turbulence field, a log-law distribution of the mean tangential velocity within the turbulent boundary layer is taken into account near the solid object. The surface tension effect is not considered.

2.2.2. Computational condition

A numerical flume setup should be identical to the experimental setup for reasonable comparisons. However, for the sake of computational efficiency, an adequate numerical flume scale should be utilized. The numerical flume in simulations is $0 \leq x \leq 15$ m and $0 \leq z \leq 0.4$ m, in which the numerical slope starts at $x = 7$ m. Therefore, a numerical reference gauge is placed at $x = 5.9$ m. Note that the following analyses are all based on this numerical tank scale. The computational grid system is discretized with two non-uniform meshes in the x-direction ($\Delta x = 0.01$ m and $\Delta x = 0.005$ m distributed before and after the sloping beach threshold) and one uniform mesh in the z-direction ($\Delta z = 0.002$ m is applied throughout the vertical domain). Thus, the total number of cell meshes is 2302×202. Additionally, total simulation time is 18 s and the Courant number is 0.3 for all cases. The corresponding time step is automatically adjusted during calculations to satisfy stability constrains by both advection and diffusion processes, in which the maximum time step is adequately chosen as 10^{-3} s compared to experimental measurements. The aforementioned computational conditions are used throughout this study.

2.2.3. Solid object treatment and the numerical approach in simulations

Appropriate treatment of a solid object in fluid plays an important role in successful model simulation. In the COBRAS model, the solid object is considered as a special fluid case with an infinite density; the partial cell approach is employed to describe the unstructured interior

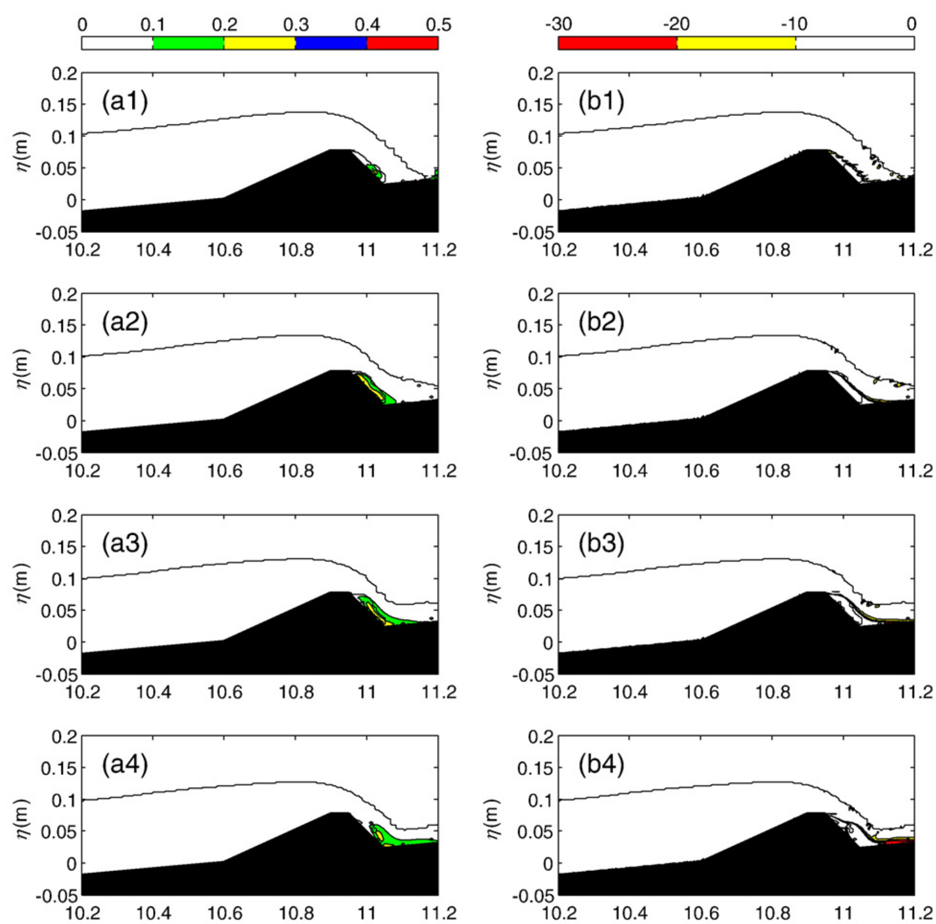

Fig. 4. Simulated (a) turbulent kinetic energy (TKE) (m/s) and (b) vorticity (m^{-1} s) fields of Type 3 case at $t = 3.11$ s (a1 and b1); 3.18 s (a2 and b2); 3.25 s (a3 and b3); 3.33 s (a4 and b4). Note, only a contour of the VOF function with $\theta = 1.0$ is presented.

obstacle and solid boundary. From a practical viewpoint, the partial cell approach can be employed to adequately construct both solid obstacles and numerical fluid with a series of conical sections using the volume–fraction ratio of water associated with an openness coefficient θ (i.e. completely occupied by an object when $\theta=0$, completely occupied by fluid when $\theta=1$, and partially occupied by an object when $0<\theta<1$). The scalar quantities of P, k and ε are obtained in each cell center, and the velocities of u and w are evaluated for each cell face. However, in a partial cell, the openness coefficient is smaller than a unit resulting in a smaller mean quantity compared to the original value (Lin, 1998; Zhang and Liu, 2008). This implies that the simulated mean physical quantities may be inadequately simulated near the solid boundary. Recalling our experiments, the pressure transducer is buried in the seawall surface, suggesting that numerical results obtained from that nearest the numerical solid may be unreasonable. Fortunately, with a sufficient mesh resolution in the calculations, the simulated pressure computed for just one cell away from the solid object is reasonable compared to that measured in the laboratory (see Section 3.3 for discussions). Furthermore, it should be emphasized that although the partial cell approach for describing numerical object is unavoidable in this study, it has relatively little influence on overall discussions of wave evolutionary behaviors.

Particularly, some important approaches are employed in the model computations. First, few experiments on solitary wave dynamics are referable to adjust the empirical coefficients in the k–ε closure model. Fortunately, the empirical values suggested by Lin and Liu (1998a,b) in describing the Reynolds stress closure model have been successfully employed to simulate various solitary wave hydrodynamics (e.g. Lin

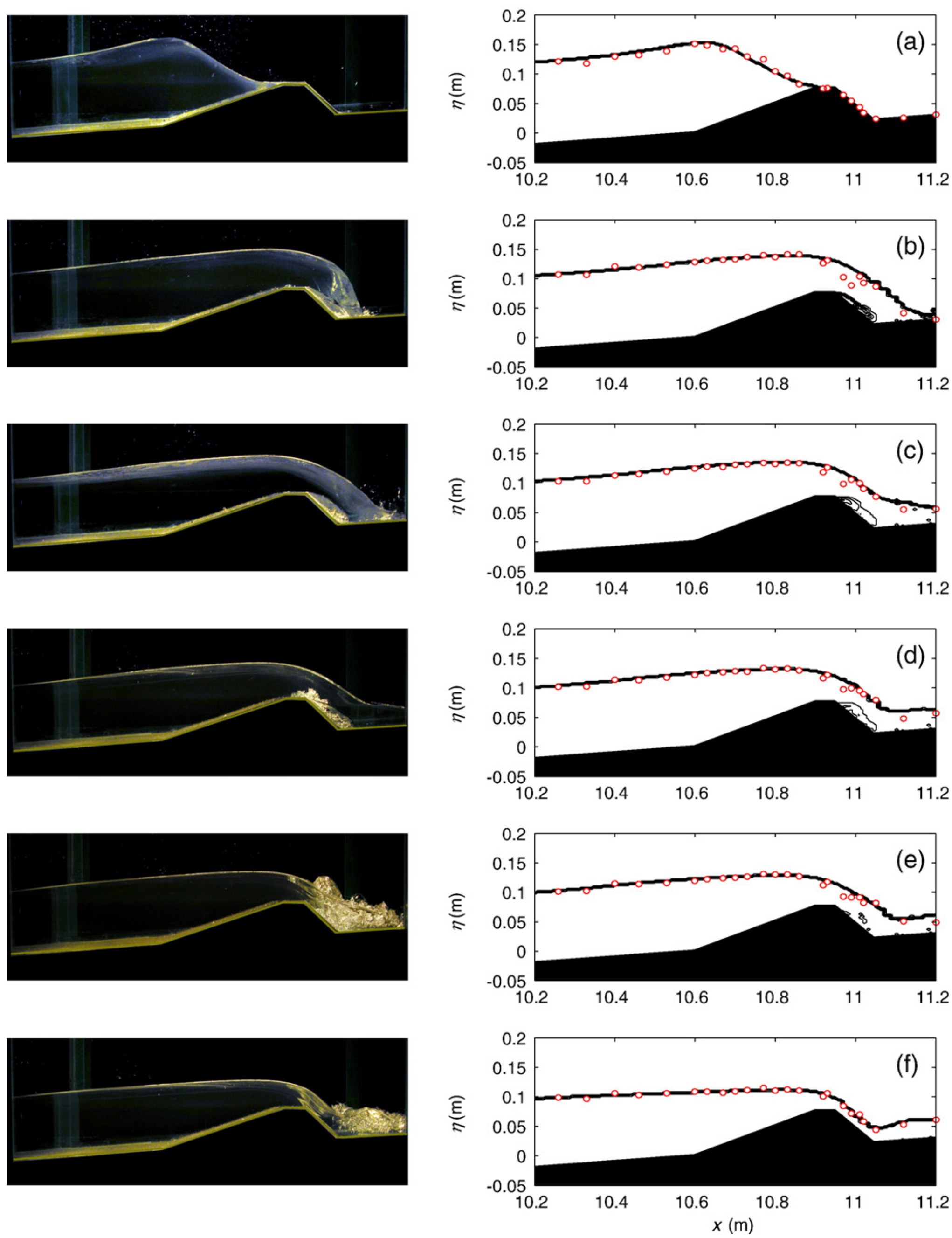

Fig. 5. Qualitative and quantitative comparisons of free surface evolution between laboratory images (left column) and measurement data (right column) (Type 3 wave: $h_o=0.256$ m, $\varepsilon=0.23$). Simulated free surface at $t=$(a) 2.79 s, (b) 3.11 s, (c) 3.18 s, (d) 3.25 s, (e) 3.33 s, (f) 3.69 s; (10 contours of the VOF function with an interval of 0.1 from 0.1 to 1.0 by black solid lines). Experimental data (○).

et al., 1999; Liu and Cheng, 2001; Liu and Al-banaa, 2004; Lin, 2004; Lin and Karunarathna, 2007). These values are used in this work. In addition, an analysis technique identical to that used by Zhang and Liu (2008), which varies the volume–fraction of water in the VOF function from 0.0 to 1.0, is also adopted to mimetically simulate the phenomenon of "air and water mixing" accompanied by laboratory breaking waves (see Figs. 2, 5 and 6). It is noted that the entrapped-air captured in breaking waves is treated as a "numerical void" and the real air–fluid interaction is not feasible in this study.

3. Results and comparisons

This section compares experimental and numerical results, including those for free surface elevation, dynamic pressure load and dynamic wave acting force. Corresponding mean wave dynamics (i.e. TKE and vorticity) are also observed based on numerical data. The discrepancies between experimental and numerical data are discussed.

3.1. Tsunami-wave description and corresponding mean wave dynamics

Figs. 2, 5 and 6 show spatial snapshots of the three wave types during their distinct evolutionary courses, including wave shoaling, breaking, impingement, run-up and overtopping. Laboratory images, measurement data and numerical results are plotted together for comparison. Based on numerical data, Figs. 3, 4 and 7 also show the corresponding mean TKE and vorticity patterns at certain evolutionary phases of interest (physical time is noted in figure captions).

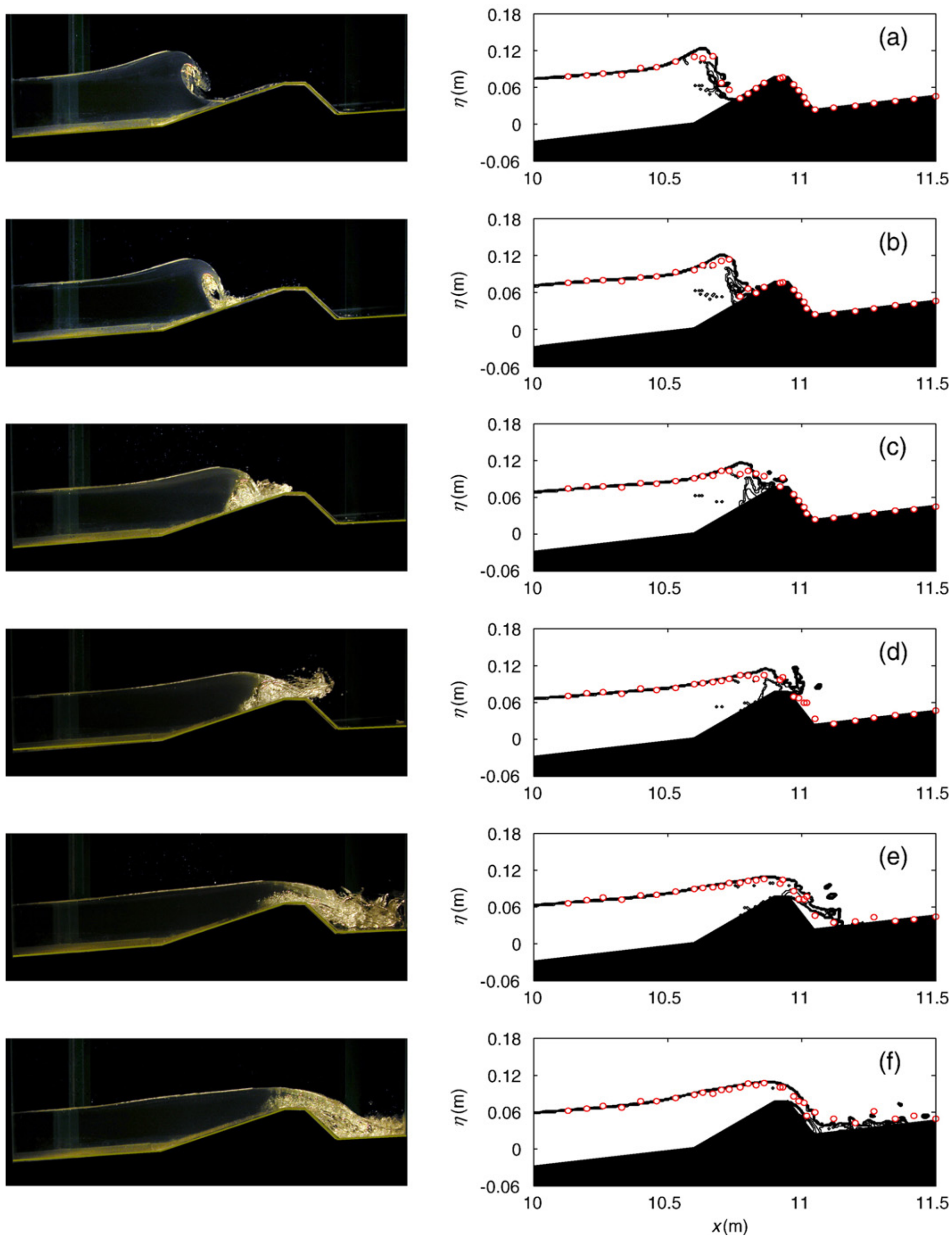

Fig. 6. Qualitative and quantitative comparisons of free surface evolution between laboratory images (left column) and measurement data (right column) (Type 2 wave: $h_o = 0.22$ m, $\varepsilon = 0.29$). Simulated free surface at $t =$ (a) 2.95 s, (b) 3.01 s, (c) 3.07 s, (d) 3.14 s, (e) 3.22 s, (f) 3.34 s; (10 contours of the VOF function with an interval of 0.1 from 0.1 to 1.0 by black solid lines). Experimental data (○).

Overall, the COBRAS model can simulate the most wave evolutionary stages. Numerical results generally agree qualitatively and quantitatively with experimental data. However, some differences exist. A time lag exists between measurement data and model results [e.g. Fig. 2(c) and (d)]. The maximum relative error of surface elevation is approximately 3% [e.g. Fig. 5(b) and (c)]. Such a discrepancy may be partly due to the unpredictability of breaking waves with naturally complex in fluid and the uncertainty of entrapped air-bubbles during repeated experiments. Although some significant air-bubble plumes were entrapped in laboratory breaking waves [e.g. Fig. 2(c), (d) and (e)], numerical results using 10 VOF-contours correlated with an openness coefficient θ of 0.1–1.0 with an interval of 0.1 shown in Figs. 2, 5 and 6 are of qualitative similarities comparing to the laboratory images. The closed contours (roughly $0.5 \leq \theta \leq 1.0$) beneath the free surface clearly indicate that some zones are not fully occupied by fluid, suggesting the "existence" of "fictitious air entrapment" phenomena in model computations. Particularly, the presence of a void would reduce dynamic wave acting pressure and further discussions will be given in Section 4. In the following sub/cross sections, mean free surface in model simulations is only represented by $\theta = 1.0$ unless stated otherwise.

3.1.1. Type 1 tsunami

In this case, the breaking wave forms a turbulent bore offshore, which then impinges upon and overtops the seawall. The incident solitary wave breaks as a plunging type, in which the wave curls over with some air [Fig. 2(a)]. The breaking wave jet initially impinges upon the front still water and releases considerable wave energy combined with a splash-up [Fig. 2(b)]; this process is evidently supported by numerical observations of turbulence generation [Fig. 3 (a2)]. The model data indicate that the maximum generated TKE is approximately of an order of $O(0.5\ \mathrm{m/s})$. Further, at the same stage, the intruded wave near the fluid surface initiates the well-known splash-up phenomenon (Li and Raichlen, 2003). The reflected jet curves clockwise back and once again collapses onshore and interacts against the incident jet in the postbreaking region [Fig. 2(b)]. Numerical results also reveal that the generated vortex of an order of $O(-10\ \mathrm{s}^{-1})$ near the bore front region was stretched through advection and eventually aggregated [Fig. 3(b1)–(b2)]. The collapsing jet simultaneously arrests considerable mixing air–fluid, subsequently resulting in a wedge-shaped bubbly fluid as a turbulent bore propagates over front still water at the front of seawall and then impinges upon the seawall [Fig. 2(c)]. The climbing bore gradually overtops the seawall and an overtopping tongue forms on the crown and then slides tardily down the seawall [Fig. 2(d) and (e)]. The analyses indicate that the maximum acting force always occurs during this phase (i.e. run-up to overtopping) — this is discussed further in Section 4. Eventually the residual fluid energy supports the remaining fluid that overtops the structure and continues propagating toward the deep inland region [Fig. 2(f)]. Meanwhile, significant reflected wave travels offshore, i.e. the substantial free surface elevates in front of the seawall. Note that after wave overtopping numerical information shows that the generated TKE/vorticity intensities do not diminish entirely, in which the residual values of TKE/vorticity are approximately 0.2 ms^{-1} and -10 s^{-1}, respectively [Fig. 3(a4) and (b4)].

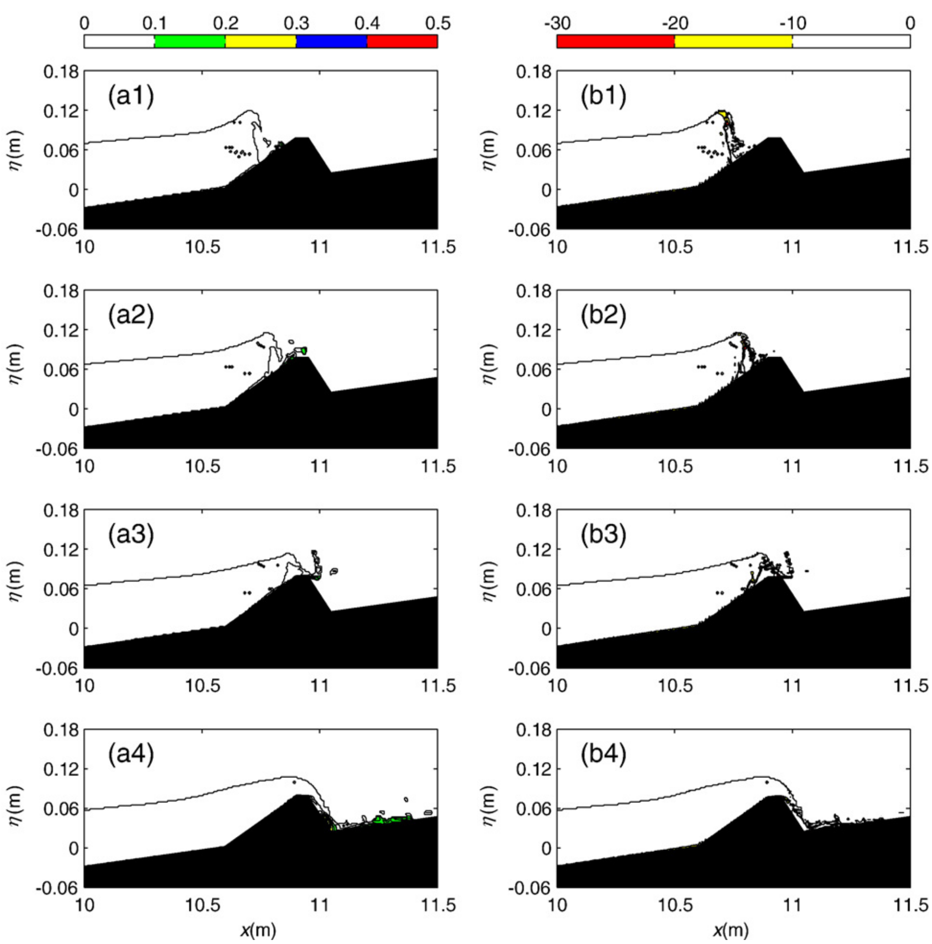

Fig. 7. Simulated (a) turbulent kinetic energy (TKE) (m/s) and (b) vorticity (m^{-1} s) fields for Type 2 wave at $t = 3.01$ s (a1 and b1); 3.07 s (a2 and b2); 3.14 s (a3 and b3); 3.34 s (a4 and b4). Note, only a contour of the VOF function with $\theta = 1.0$ is presented.

3.1.2. Type 2 tsunami

For the Type 2 wave, the wave collapses directly upon the seawall and an overtopping flow is subsequently generated. With the same plunging breaker as that for Type 1 [Fig. 6(a)], the leading breaking front also captures considerable air and starts impacting the seawall [Fig. 6(b)]. The wave evolutionary comparison of Type 1 and Type 2 [Figs. 2(b) and 6(b)] indicates that the breaking wave finger interacting with the front shoreline occurs in a relatively narrow space [Fig. 6(b) and (c)]. This generates a transient splash-up for a reflected jet not fully developed, and the seawall also contributes to strong reflection increasing the violence of the recollision of the coming breaking wave and reflected jet [Fig. 6(d)]. The extruded jet therefore has a significant velocity due to a high pressure gradient with a considerable impulsive wave momentum, resulting in a relatively stronger overtopping flow that spills into the deeper leeward region compared to that for Type 1 [Figs. 2(d), (e) and 6(d), (e)]. Note that the generated TKE/vorticity during these stages is generally concentrated within the resulting overtopping tongue [Fig. 7(a2)–(a3) and (b2)–(b3)]. The corresponding values are relatively small compared to those for the Type 1 wave. Further, the overland flow behind the seawall causes an onshore turbulent bore, resulting in a distinct reversal flow with TKE and vorticity generations, in which waves first climb up the crown and then slide downstream gradually. In this case, the intensity of simulated wave dynamics cannot be quantified easily because of the thin flow width behind the seawall. It is noted that

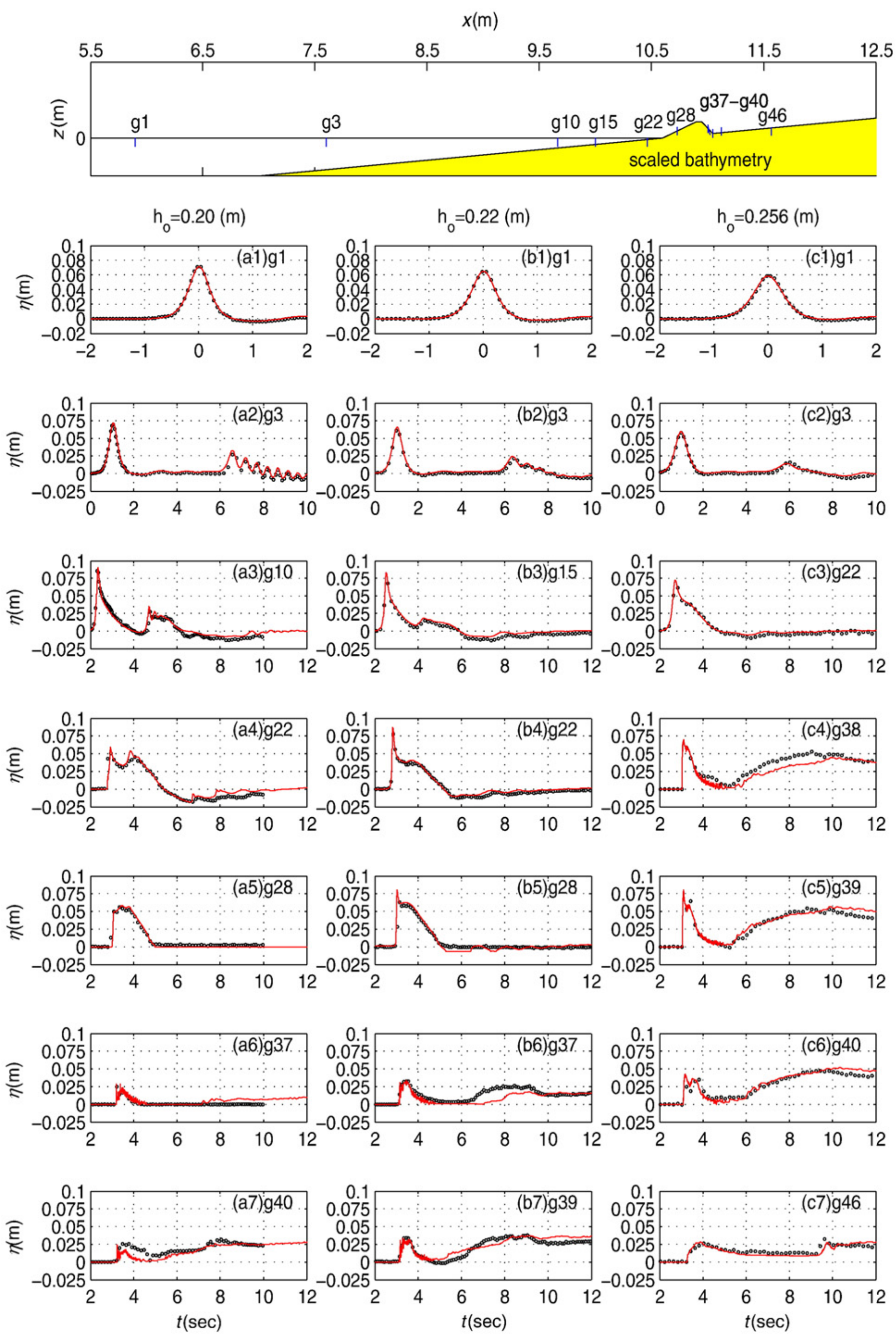

Fig. 8. Time history comparison of free surface elevation due to waves interacting against seawall. Simulated surface elevation (solid line); experimental data (○). In the present figure, g1(x = 5.9 m); g3(x = 7.6 m); g10(x = 9.644 m); g15(x = 10 m); g22(x = 10.462 m); g28(x = 10.732 m); g37(x = 11.005 m); g38(x = 11.024 m); g39(x = 11.045 m); g40 (x = 11.12 m); g46(x = 11.57 m).

in this case the maximum impulsive wave force may not always occur at the moment of wave impact.

3.1.3. Type 3 tsunami

In this case, the wave straightforwardly overtops the seawall crown and subsequently collapses behind the seawall. A distinct clockwise vortex is generated after the wave breaks, in which considerable air is entrapped [Fig. 5(b)]. The generated vortex initially climbs up toward the crown and then propagates downstream gradually through advection and diffusion processes [Fig. 5(b)–(d)]. Particularly, the reverse flow forms a second breaking wave as a hydraulic jump that interacts with the coming tail wave, which increases the complexity of the flow field [Fig. 5(d) and (e)]. Numerical data indicate that the local fluid particles are accelerated during this phase. Additionally, numerical simulation shows that within these stages, the generated TKE and vorticity are approximately of $O(0.1–0.2\ \mathrm{ms}^{-1})$ and $O(-10\ \mathrm{s}^{-1})$, respectively, which generate the same evolutionary behaviors as that for free surface. The maximum wave acting force of this type wave (i.e. $R_c = 0$) occurs during the stage before the wave breaks. Notably, the wave dynamics of this case (i.e. overtopping flow behind the seawall) is discussed further in Section 4.2 via additional laboratory and numerical observations.

3.2. Free surface elevation

Fig. 8 shows the agreements between laboratory data and numerical results of time histories of local free surface elevation

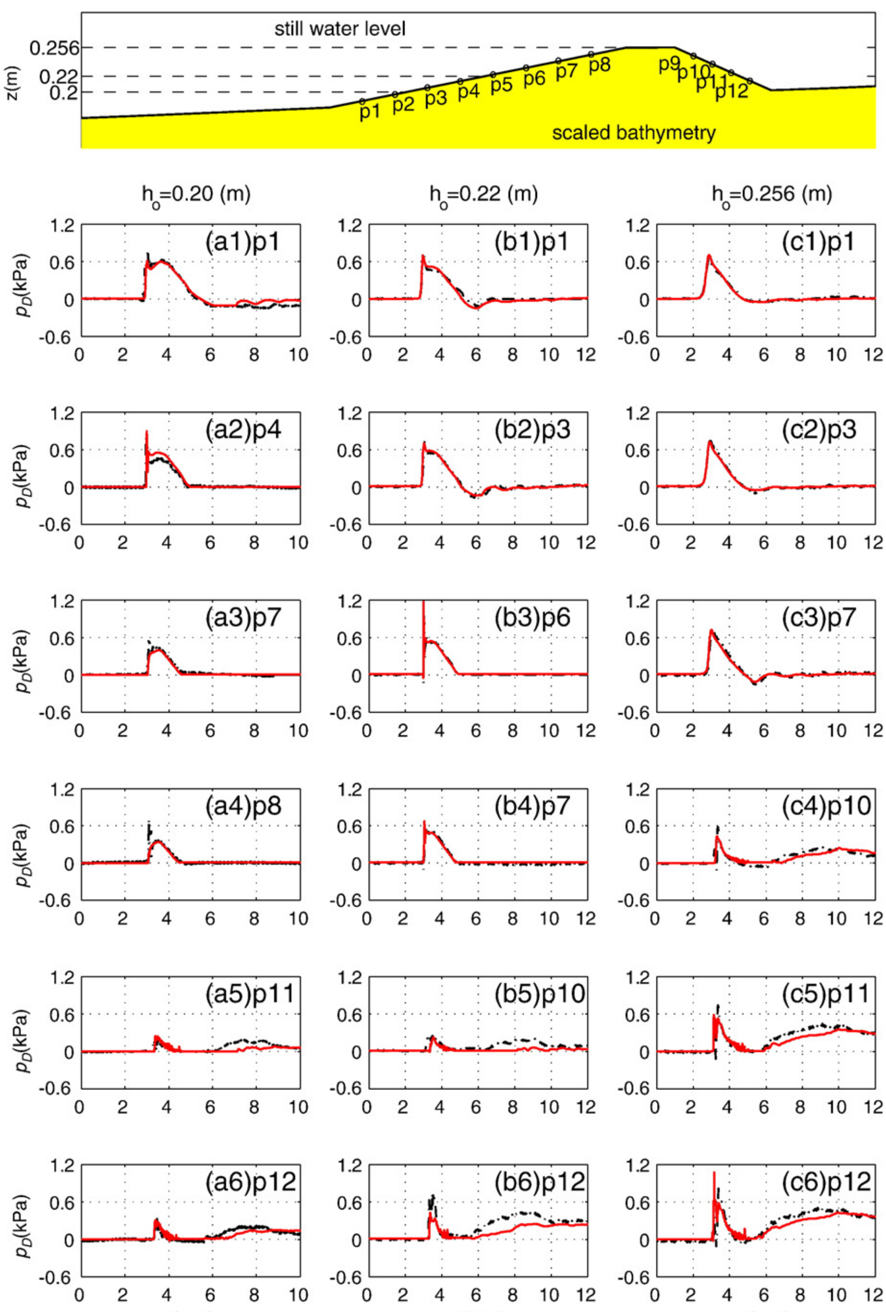

Fig. 9. Time history comparison of dynamic pressure due to waves impacting the seawall. Simulated dynamic pressure (red solid line); experimental data (black dash–dot line). For locations of each pressure transducer, refer to Fig. 1.

along the flume. A sequence of oscillatory waves due to reflection by the seawall at time $t>6$ s is clearly observed [Fig. 8(a2), (b2) and (c2)]. The reflected waves decrease as the freeboard decreases. A possible explanation of this behavior is that in the bore formation and impingement case (i.e. Type 1), the wave breaks earlier compared than in the other two cases, such that the wave breaks before the seawall and losses considerable wave energy, therefore contributing to a weak impulsive overturning jet momentum (see Section 3.1.1). The resultant powerless jet flow yields the most incident wave energy being blocked before the seawall and continuously interacts with the seawall front, producing a leading reflected wave. In the meantime, an additional reflected tail wave is generated by the retreating wave that does not overtop the crown completely [i.e. Fig. 2(e) and (f)]. Further, time history data of free surface elevation shown in Fig. 8(c4)–(c6) clearly respond the second breaking wave generated behind the seawall, in which distinct surface variations exist after the peak in the data.

3.3. Dynamic wave pressure load

Before comparing pressure results, a numerical issue related to pressure must be clarified. The present simulated pressure was occasionally very large at a certain time step, Δt, with an error of O (100%), which is greater than that for the experimental data. This

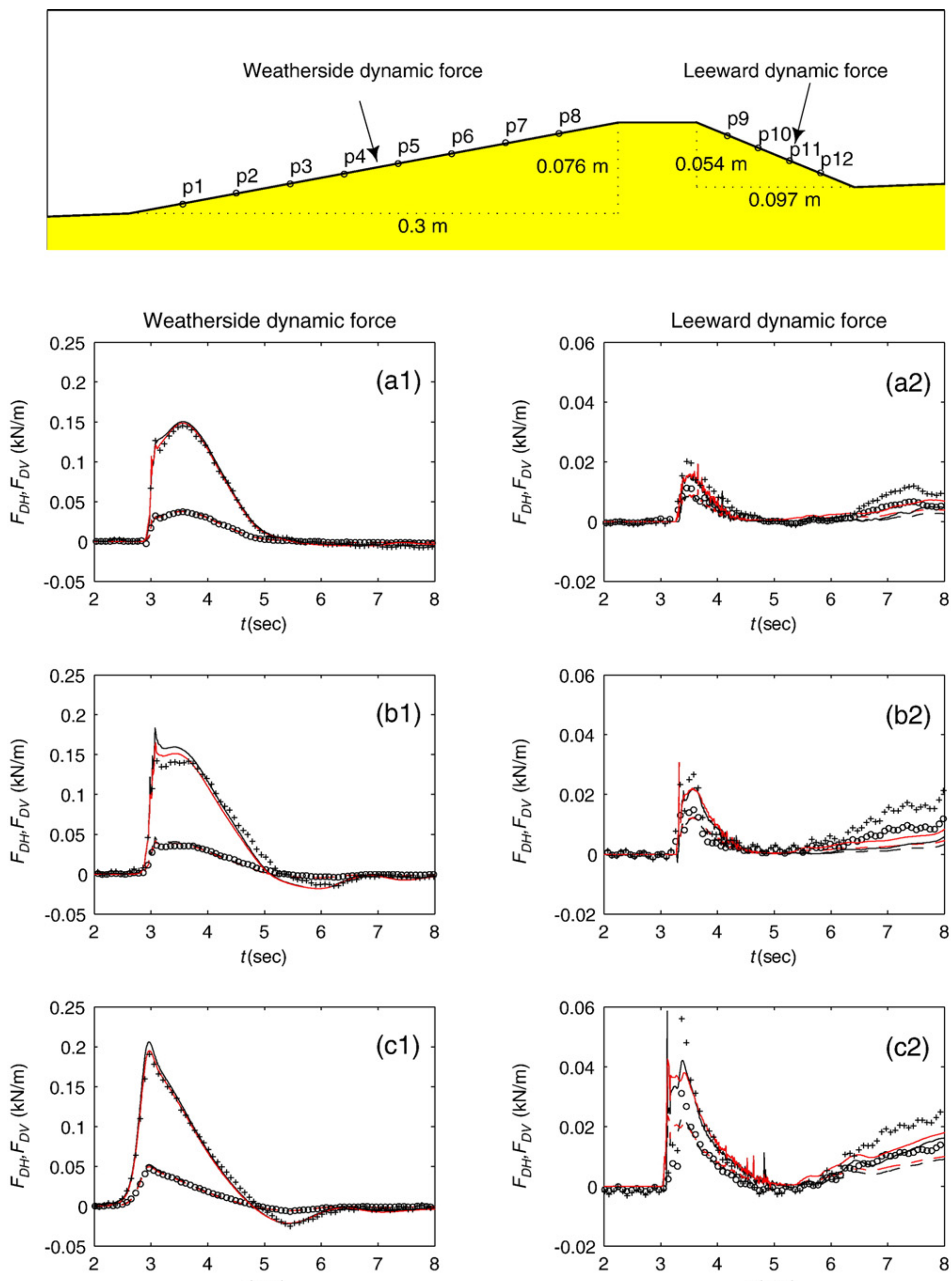

Fig. 10. Comparison of dynamic wave force due to waves interacting against the seawall. (a1) and (a2): $h_o=0.20$ m, $\varepsilon=0.35$; (b1) and (b2): $h_o=0.22$ m, $\varepsilon=0.295$; (c1) and (c2): $h_o=0.256$ m; $\varepsilon=0.228$. The COBRAS model with a coarse grid in the horizontal component (black solid line); the COBRAS model with a coarse grid in the vertical component (black dashed line); the COBRAS model with a fine grid in the horizontal component (red solid line); the COBRAS model with a fine grid in the vertical component (red dashed line); and experimental data: horizontal component force (+); and vertical component force (○).

results from the fact that the VOF function is solved close to obstacles or where waves break, suggesting that such simulation results may be unreasonable. From a physical perspective, a pressure spike is possibly observed due to wave impacting the obstacle. Therefore, the unusual pressure spike at a certain time step of each numerical pressure gauge is reconsidered on a physical basis. That is, these fictitious spikes of pressure gauges are removed from simulation results in the case of the wave not directly impinging upon these gauges. Most importantly, this change would nearly not affect the following force calculation.

As shown in Fig. 9, simulated dynamic pressure results are in agreement with experimental data, suggesting that the partial cell effect (see Section 2.2.3) does not significantly affect the simulation results. The reconsideration of fake pressure spikes is reasonable. However, some discrepancies should be clarified. First, the COBRAS model did not adequately simulate the propagating bore head impingement with a maximum error of approximately 20%. The reason is based on the difference between breaking bore formation and impingement [i.e. Fig. 2(c) and (d)]. Additionally, the COBRAS model underestimates/overestimates pressure spikes at certain locations where breaking wave impingement is expected [i.e. Fig. 9(a4) and (b3)]. The corresponding maximum errors of that for pressure spikes are approximately 72% and 23%, respectively. Although these errors are considerable, ensuring that wave impingement locations and magnitudes are the same during repeat experiments is difficult due to the complexity of breaking waves. Section 1 pointed out similar laboratory observations by Chen and Melville (1988).

For all three wave cases, the time histories of dynamic pressure are similar for the sudden spike and slow decay under wave impingement. The smaller increase rate to maximum dynamic pressure and larger decay rate to minimum dynamic pressure exist as the freeboard decreases. For Type 3 wave, pressure data behind the seawall [Fig. 9(c4), (c5) and (c6)] exhibit a "sub-atmosphere pressure" phenomenon (see Fig. 4 in Bullock et al. (2007)). As reported by Bullock et al. (2007), such pressure behaviors are generated in high aeration regions, in which a significant amount of air is entrapped by the surrounding fluid, resulting in a relatively long duration of air–fluid interaction. Further, the air pocket or bubble plume also lead to severe damping oscillation following the pressure spikes [Fig. 9(c4)–(c6)], suggesting that the high aeration region may cause well-known cavitation damage and also generates the pressure continuously acting on the landward structure. Section 4.2 will show some experimental data that support this statement. Note that some negative

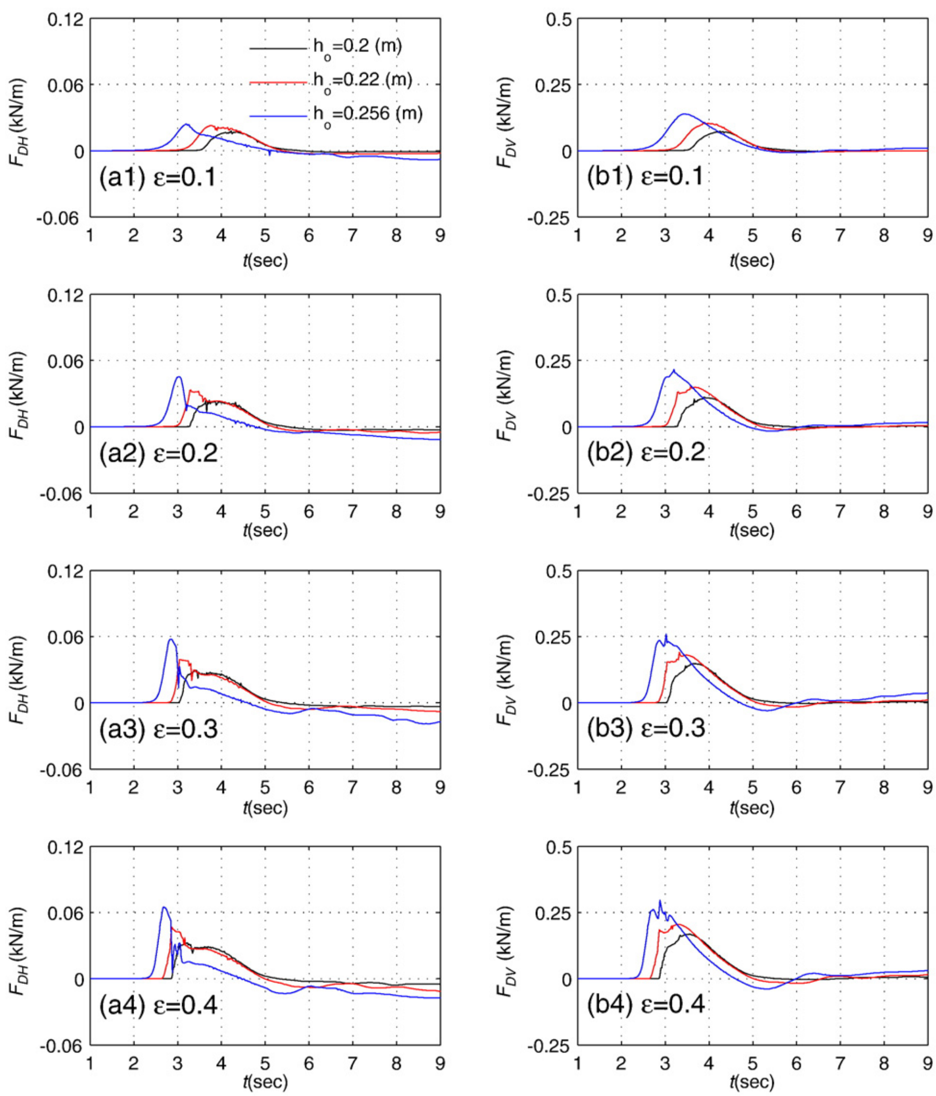

Fig. 11. Simulated dynamic net wave force (DNWF) per unit width acting on the seawall. (a), Horizontal component (F_{DH}); and (b), vertical component (F_{DV}). For the definition of the DNWF, refer to Section 4.

pressures exist in the front seawall face [Fig. 9(c1)–(c3)]. This feature is caused by the depression of the free surface due to wave propagation, which differs from that induced by entrapped air.

3.4. Dynamic wave force load

The dynamic wave force per unit width acting on the structure was obtained by integrating dynamic pressure data along the seawall surface. Note that the calculated force acting on the crown is absent in the comparisons because no pressure gauges are available on the seawall crown in experiments. To test the simulated force sensitivity, two pressure transducer resolutions are employed for comparison: (1) a coarse resolution — 8 transducers on the weather side and 4 on the leeward side of the structures, which is the same as experiments; and (2) a fine resolution — 30 transducers on the weather side and 20 on the leeward side of the structures, in which transducers are spaced uniformly with $\Delta x = 0.01$ m between any two transducers. All calculated results are summarized in Fig. 10. Note that the above setup is adopted for numerical pressure transducers only. The computational mesh does not change.

Evidently, numerical results with two gauge resolutions agree well with laboratory data. It is found that when using fine pressure resolution, simulation results can capture laboratory data with increased accuracy. Simulation results also show that the vertical dynamic force on the weather side seawall is markedly larger than the horizontal dynamic force due to larger projected area of the seawall. Additionally, the smaller increasing rate to the maximum and larger decaying rate to the minimum dynamic force as the freeboard decreases are revealed, which exhibit the same behavior as local dynamic pressures.

4. Numerical experiments and overall discussion

Section 3 demonstrates that the COBRAS model is capable of simulating a solitary wave impinging and overtopping a seawall on a sloping beach. In this section, a set of numerical experiments is performed to investigate the dynamic net wave force (DNWF) acting on the seawall. The effects of freeboard and wave nonlinearity are considered. The DNWF is acquired by summing the numerical wave force data acting on the weather and leeward sides of the seawall. The onshore ($+x$) and downward ($-z$) acting forces in the horizontal and vertical directions are defined as positive. In the following simulations, the fine resolution setup of pressure gauges is adopted (see Section 3.4). However, in addition to the total 50 pressure transducers placed on seawall slopes, 4 transducers are placed on the crown for completeness. The wave nonlinearities chosen in numerical experiments are 0.1, 0.2, 0.3 and 0.4, with the same three water depths as those used in experiments ($h_o = 0.2$, 0.22 and 0.256 m), indicating that 12 cases in total can be discussed together. All numerical parameters are identical to those in the previous model setup. Experimental observations are used to study the kinematic and dynamic properties of vortex generation/evolution behind the seawall, as mentioned in the Type 2 and 3 cases, in which the dynamic effect of entrapped air-bubbles is briefly addressed using experimental and numerical observations.

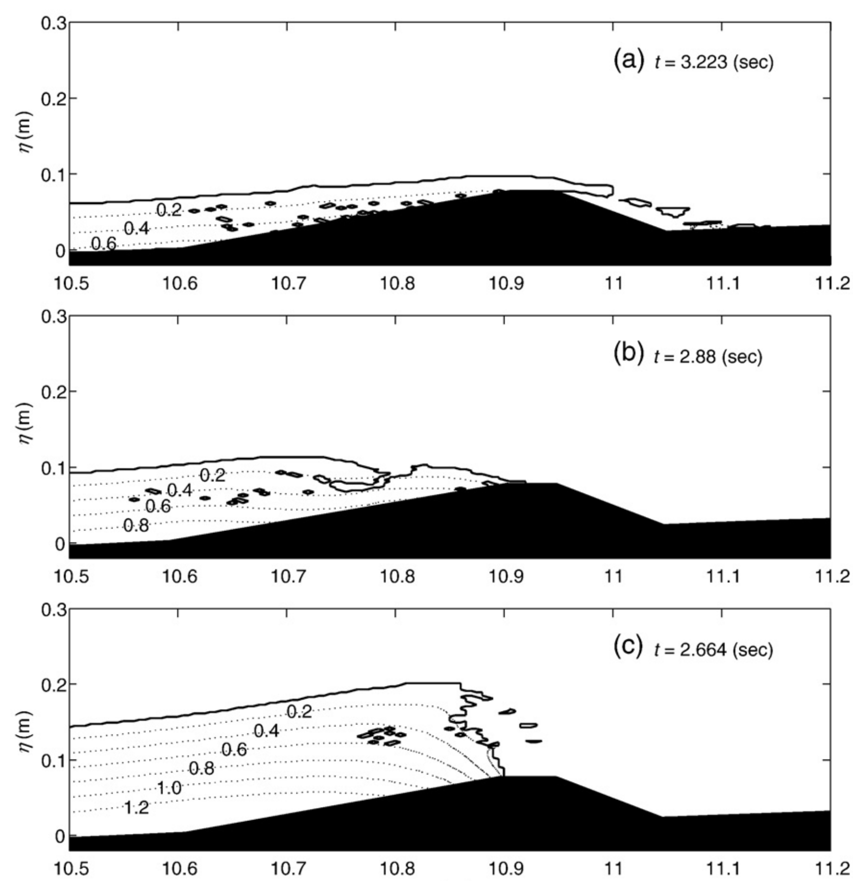

Fig. 12. Snapshots of simulated free surface (black solid line) and wave pressure field (contour lines with an interval of 0.2) (unit: kPa) at the moment when the horizontal DNWF peaks (see Fig. 11). (a), $\varepsilon = 0.4$, $h_o = 0.2$ m; (b), $\varepsilon = 0.4$, $h_o = 0.22$ m; (c), $\varepsilon = 0.4$, $h_o = 0.256$ m.

4.1. Dynamic net wave force (DNWF) and the time at which maximum DNWF occurred

Fig. 11 systematically summarizes simulated DNWF for all cases; the left and right columns list horizontal and vertical force components, respectively. Note that the numerical results indicate that all simulated cases of $\varepsilon = 0.1$ do not break before the seawall (i.e. no significant turbulence is generated during the shoaling course) and the cases of $\varepsilon = 0.4$ always break after they shoal upon the seawall. Clearly, for the same wave nonlinearity, the seawall experiences the net force earlier as the water depth increases; this is easily interpreted using an approximately long wave speed of shallow water-wave theory. The DNWF increases as wave nonlinearity increases for all cases. For the case of $\varepsilon = 0.1$, both the horizontal and vertical forces appear as quite smooth shapes because no wave breaking occurs; cases with relatively higher nonlinearity have significantly more complicated patterns.

Two interesting phenomena are observed. (1) For the same water depth, significant force decay with oscillation after the first data spike increases as wave nonlinearity increases, especially at *ca.* $2.8 < t < 3.1$ s for the case of $h_o = 0.256$ m with $\varepsilon = 0.4$ [Fig. 11(a4) and (b4)]. This is because that as wave nonlinearity increases, the "numerical air-void" increases following the increase in vortex size behind the seawall, which substantially reduces the wave dynamic pressure. Detailed discussions are given in Section 4.2. (2) For the same wave nonlinearity, negative forces are revealed markedly as water depth increases. This is simply caused by the retreating wave propagating offshore; thus, the negative values of DNWF are obvious.

Notably, for the same wave nonlinearity our numerical results show that DNWF peaks when the freeboard is minimum in all cases, suggesting that the coastal structures due to a rising sea level are exposed to significant risk of extreme wave attacks. A similar conclusion for a solitary wave impinging upon a vertical structure (no overtopping phenomenon) built upon a sloping beach was also obtained by Xiao and Huang (2008).

In practice, the time at which the DNWF is maximum on the seawall occurs is of great interest from an engineering prospective. Special attention is therefore paid to the maximum horizontal DNWF as it can represent a typical effect due to wave impingement. Fig. 12 shows typical cases of $\varepsilon = 0.4$ for three water depths in the simulations, in which the free surface snapshots and corresponding pressure fields are presented at the instant when the horizontal maximum DNWF occurred. It is seen that with the same nonlinearity, the wave evolutionary stages differ markedly. The onset of maximum acting force for deeper water depth starts its overtopping process [Fig. 12(c)], and, conversely, the waves at relatively smaller water

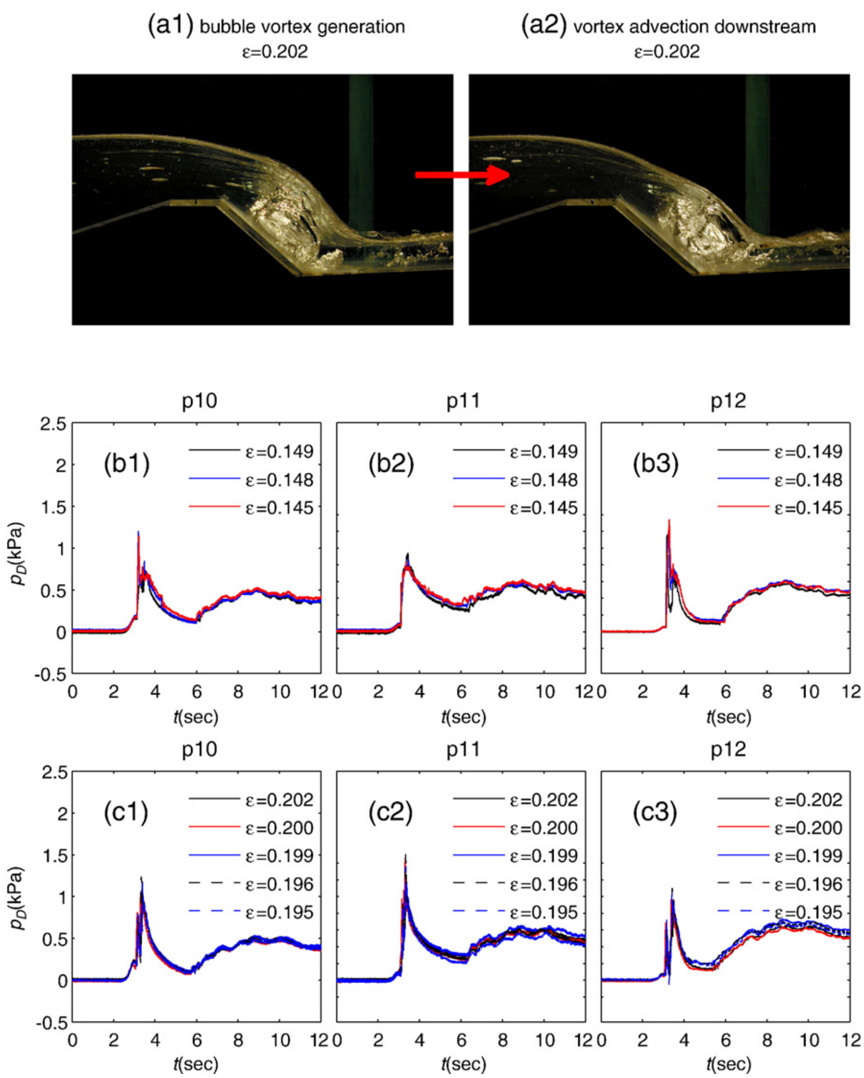

Fig. 13. Additional experiments ($h_o = 0.256$ m) to verify vortex generation and the corresponding dynamic pressure behind the seawall. Subplots (a1 and a2): laboratory snapshots of bubble-vortex generation and advection behind the seawall. Subplots (b1–b3) and (c1–c3): experimental data of the time history of dynamic pressure on the leeward seawall surface.

depths have already broken and climbed upon the seawall [Fig. 12(a) and (b)]. Generally, numerical results indicate that, based on the present seawall topography, the moment of maximum DNWF mostly occurred when the surface elevation near seawall increases up to certain elevations (i.e. run-up to overtopping stages). The impingement of a breaking wave may not necessarily lead to the maximum DNWF. In the simulations, maximum DNWF only occurred when the wave impinged upon the seawall only for the case of $\varepsilon = 0.3$ with $h_o = 0.22$ m.

4.2. Vortex behavior and its corresponding wave dynamics behind the seawall

Fig. 13 presents additional experimental results ($h_o = 0.256$ m) for vortex generation/evolution behaviors behind the seawall [Fig. 13(a1) and (a2)] and the corresponding dynamic pressure response along the leeward seawall surface [Fig. 13(b1)–(b3) and (c1)–(c3)]. Experimental wave conditions and gauge locations are given in each figure. Evidently, as the wave collapses behind the seawall, a distinct clockwise vortex is

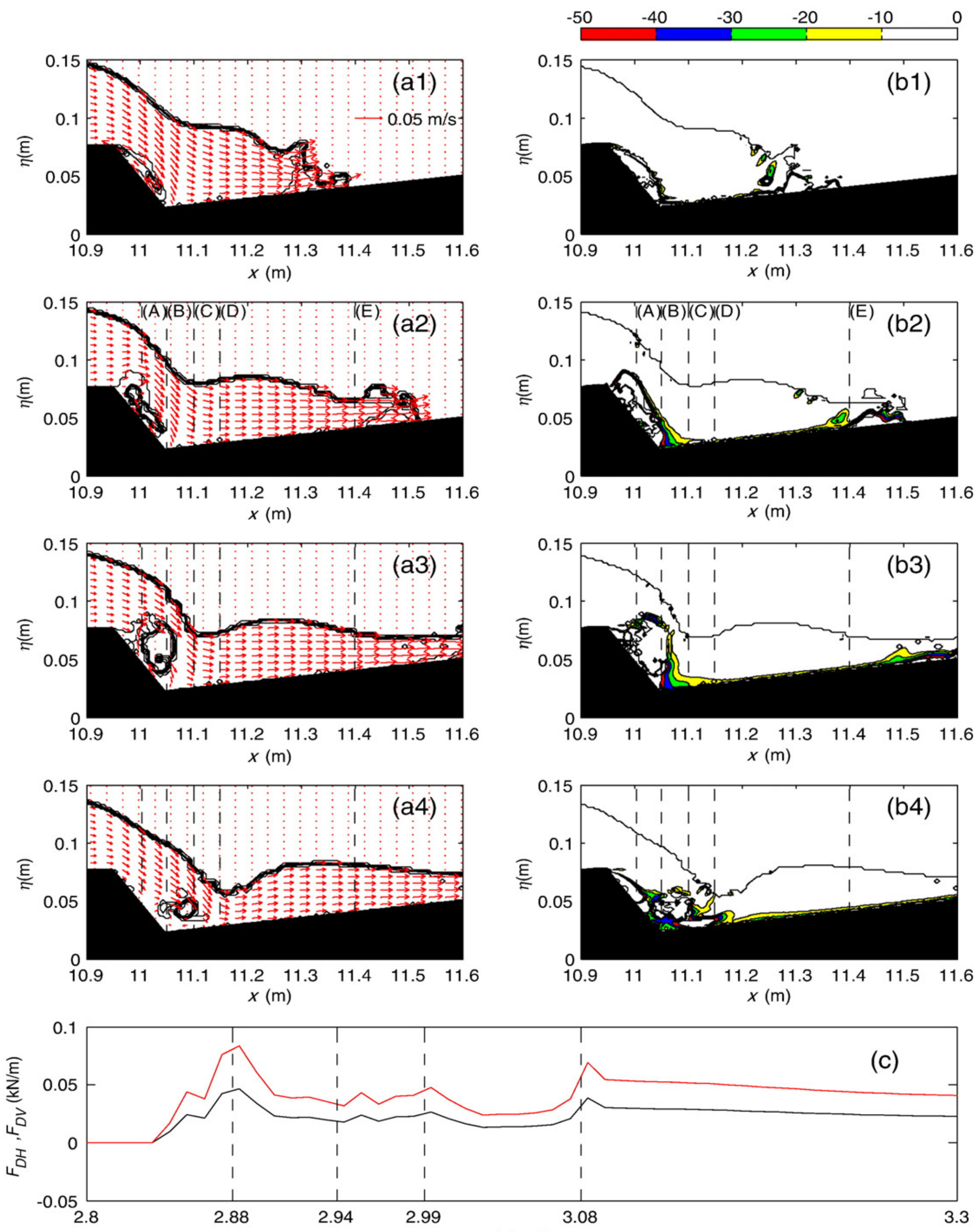

Fig. 14. Simulated overtopping wave behaviors ($h_o = 0.256$ m, $\varepsilon = 0.4$) behind the seawall at $t = 2.88$ s (a1 and b1), $t = 2.94$ s (a2 and b2), $t = 2.99$ s (a3 and b3) and $t = 3.08$ s (a4 and b4). (a1)–(a4): free surface evolution (10 contours of the VOF function with an interval of 0.1 from 0.1–1.0 by black solid lines) and mean velocity fields (red arrow). (b1)–b(4): free surface evolution (1 contour of the VOF function 1.0 by a black solid line) and mean vorticity pattern (color contour with an interval of −10 from −50 to 0 s^{-1}). Subplot (e) shows time history of the corresponding DNWF on the leeward seawall surface: FDH (black line) and FDV (red line). The physical times of subplots (a1)–(a4) are also plotted in (e) by black dashed lines.

generated, in which considerable air is also entrapped. The bubbly-vortex initially moves up to the crown [Fig. 13(a1)], and subsequently propagates downstream through advection and diffusion [Fig. 13(a2)]. Experimental observations indicate that the size of the vortex increases as wave nonlinearity increases and the sub-atmosphere phenomena are more pronounced in relatively stronger wave nonlinearity cases [Fig. 13 (b3) and (c3)]. Experimental observations also indicate that pressure spikes decrease significantly near the toe of the leeward slope, where the vortex initially forms.

Especially, we speculate that a negative dynamic pressure may have occurred when wave nonlinearity exceeded a certain threshold value, in which the cavitation damage may occur. Unfortunately, this result cannot be robustly confirmed due to the experimental limitations associated with the wavemaker stroke. Therefore, we present the numerical results for the case of $\varepsilon = 0.4$ with the same water depth of $h_o = 0.256$ m. A set of snapshots on free surface evolution with 10 contours of the VOF function and vorticity filed at four distinct time instants are drawn in Fig. 14(a1)–(a4), whereas vorticity patterns are shown in Fig. 14(b1)–(b4). It shows that a void with vortex motion remarkably forms when the wave breaks behind the seawall, in which the adjacent velocity field exhibits a clockwise rotation pattern. The intensity of generated vorticity is approximately of orders of $O(-50$ to $-10\ \mathrm{s}^{-1})$, implying that significant air is entrapped in real laboratory experiments and may cause the cavitation phenomenon. In addition, the decrease in the corresponding force acting upon the leeward seawall is also observed during the void (vortex) evolutionary processes [Fig. 14(c)], which corresponds to our previous findings.

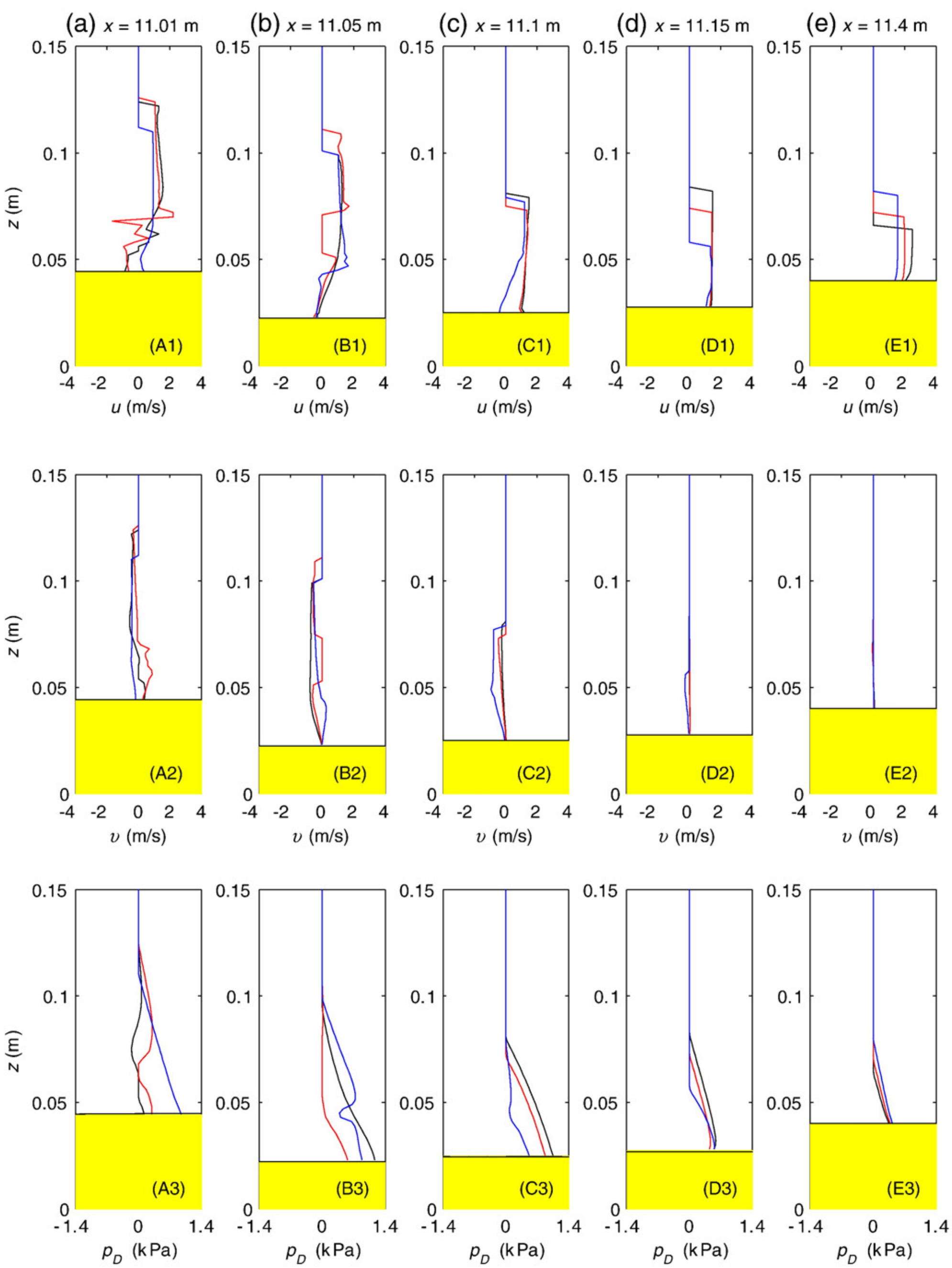

Fig. 15. Corresponding wave dynamic behaviors of horizontal velocity u (m/s) (A1–E1), vertical velocity v (m/s) (B2–E2) and dynamic pressure PD (kPa) (A3–E3) in Fig. 14(b), (c) and (d) [black line ($t = 2.944$ s), red line ($t = 2.994$ s) and blue line ($t = 3.084$ s)]. Note, measurement locations are given by black dotted lines [in Fig. 14(b), (c) and (d)].

To see it more clearly, Fig. 15 presents the corresponding snapshots of wave dynamics obtained at five cross sections in Fig. 14 (i.e. by black dotted line). The results shown in Fig. 15 indicate that two interesting phenomena exist. (1) The wave dynamic pressure at a certain cross section reduces significantly following the void evolutionary courses [Fig. 15(A3)–(C3)]. The vertical pressure distributions above the void are almost zero [e.g. $z > 0.046$ m in Fig. 15(B3)]. At this moment, the fluid upon the void can be interpreted as a free jet in air, in which pressure corresponds to the gauge pressure. As the void vanishes, the pressure distribution is generally hydrostatic [Fig. 15(D3) and (E3)]. (2) The secondary breaking behavior instantaneously contributes to the increase in vertical velocity [Fig. 15(B2) and (C2)] and the horizontal velocity is comparatively without effect [Fig. 15(B1) and (C1]. Furthermore, it is seen that almost only the horizontal velocity component within the leading bore front exists, the velocity distribution of which is uniform [Figs. 15(D1), (E1) and (D2) and (E2)].

5. Conclusions

In this paper, tsunami-like solitary waves impinging and overtopping an impermeable seawall on a 1:20 sloping beach are investigated. New laboratory experiments are presented for three typical cases. The COBRAS model is successfully validated by experimental data. Numerical data are employed to examine certain wave dynamics that is unavailable in experiments. An application is constructed via a set of numerical experiments to study the DNWF acting on the seawall. The effects of wave nonlinearity and freeboard due to waves interacting against the seawall are identified. The distinct vortex motions behind the seawall correlated with entrapped air effects are also reported from both experimental and numerical observations. It should be highlighted that the present experiments and simulations generated data for solitary waves impinging and overtopping a coastal object; such data are unavailable in literature. The experimental data can be utilized for further numerical model development and validation.

For the seawall topography in this study, it is found that the maximum DNWF due to waves impacting the seawall usually occurred at the moment when surface elevation near the seawall increases to a certain elevation (i.e. run-up to overtopping stages). The impinging behavior of the breaking wave may not cause maximum DNWF. The simulation results indicate that for the same wave nonlinearity our numerical results show that DNWF peaks when the freeboard is minimum in all cases, suggesting that coastal structures have a high risk of extreme wave attacks due to the rising sea level. Wave dynamics due to different impinging waves acting against the object may also lead to substantial structural damage and instability. Additionally, entrapped air combined with fluid vortex evolution behind the seawall experimentally/numerically indicates that the presence of air-cave/void that reduces the wave dynamic pressure. However, detailed investigations of the interaction between real fluid, structure and air are not feasible using the COBRAS model. Additional experiments and numerical studies are warranted.

Acknowledgements

Professor Philip L.-F. Liu and Mr. C.-P. Huang of Cornell University are appreciated for their valuable information concerning the COBRAS model, as well as Mr. W.-C. Chen and Dr. K.-S. Hwang for their laboratory assistance and discussion. The anonymous reviewers are commended for their valuable comments and suggestions. The second author thanks the Tainan Hydraulics Laboratory for supporting this research. The authors would like to thank the National Science Council of Taiwan for financially supporting this research under Contract No. NSC 96-2628-E006-249-MY3. The Research Center of Ocean Environment and Technology, National Cheng Kung University, is also appreciated for its support under the Tsunami-wave project. Mr. Ted Knoy is appreciated for his language assistance.

References

Bullock, G.N., Obhrai, C., Peregrine, D.H., Bredmose, H., 2007. Violent breaking wave impacts. Part 1: Results from large-scale regular wave tests on vertical and sloping walls. Coast. Eng. 54, 602–617.
Carrier, G.F., Wu, T.T., Yeh, H., 2003. Tsunami run-up and draw-down on a plane beach. J. Fluid Mech. 475, 79–99.
Chang, K.-A., Hsu, T.-J., Liu, P.L.-F., 2001. Vortex generation and evolution in water waves propagating over a submerged rectangular obstacle. Part I: Solitary waves. Coast. Eng. 44, 13–36.
Chang, Y.-H., Hwang, K.-S., Hwung, H.-H., 2009. Large-scale laboratory measurements of solitary wave inundation on a 1:20 slope. Coast. Eng. 56, 1022–1034.
Chen, E.S., Melville, W.K., 1988. Deep-water plunging wave pressures on a vertical plane wall. Proc. R. Soc. Lond. A 417, 95–131.
Dodd, N., 1998. Numerical model of wave run-up, overtopping, and regeneration. J. Waterw. Port Coast. Ocean Eng. 124 (2), 73–81.
Garcia, N., Lara, J.L., Losada, I.J., 2004. 2-D numerical analysis of near-field flow at low-crested permeable breakwaters. Coast. Eng. 51, 991–1020.
Goring, D.G., 1978. Tsunamis — the Propagation of Long Waves onto a Shelf. Rep. No. KH-R-38. California Institute of Technology, Pasadena, Calif.
Grilli, S.T., Losada, M.A., Martin, F., 1994. Characteristics of solitary wave breaking induced by breakwaters. J. Waterw. Port Coast. Ocean Eng. 120 (1), 74–92.
Guanche, R., Losada, I.J., Lara, J.L., 2009. Numerical analysis of wave loads for coastal structure stability. Coast. Eng. 56, 543–558.
Hsiao, S.-C., Hsu, T.-W., Lin, T.-C., Chang, Y.-S., 2008. On the evolution and run-up of breaking solitary waves on a mild sloping beach. Coast. Eng. 55, 975–988.
Hu, K., Mingham, C.G., Causon, D.M., 2000. Numerical simulation of wave overtopping of coastal structures using the non-linear shallow water equations. Coast. Eng. 41, 433–465.
Hughes, S.A., 1993. In: Liu, P.L.-F. (Ed.), Physical Models and Laboratory Techniques in Coastal Engineering. In: Adv. Series Ocean Eng., vol. 7. World Scientific, Singapore.
Kato, F., Inagaki, S., Fukuhama, M., 2005. Wave force on coastal dike due to tsunami. Porc. 25th ICCE, Orlando, pp. 5150–5161.
Kobayashi, N., Raichle, A.W., 1994. Irregular wave overtopping of revetments in surf zones. J. Waterw. Port Coast. Ocean Eng. 120 (1), 56–73.
Lara, J.L., Garcia, N., Losada, I.J., 2006a. RANS modelling applied to random wave interaction with submerged permeable structures. Coast. Eng. 53, 395–417.
Lara, J.L., Losada, I.J., Liu, P.L.-F., 2006b. Breaking waves over a mild gravel slope: experimental and numerical analysis. J. Geophys. Res. 111, C11019. doi:10.1029/2005JC003374.
Lara, J.L., Losada, I.J., Guanche, R., 2008. Wave interaction with low-mound breakwaters using a RANS model. Ocean Eng. 35, 1388–1400.
Lee, J.J., Skjelbreia, E., Raichlen, F., 1982. Measurement of velocities in solitary waves. J. Waterw. Port Coast. Ocean Eng. 108 (WW2), 200–218.
Li, Y., Raichlen, F., 2003. Energy balance model for breaking solitary wave runup. J. Waterw. Port Coast. Ocean Eng. 129 (2), 47–59.
Lin, P., 1998. Numerical modeling of breaking waves. Ph.D dissertation, Cornell University, Ithaca, USA.
Lin, P., 2004. A numerical study of solitary wave interaction with rectangular obstacles. Coast. Eng. 51, 35–51.
Lin, P., Karunarathna, S.A.S., 2007. Numerical study of solitary wave interaction with porous breakwaters. J. Waterw. Port Coast. Ocean Eng. 133 (5), 352–363.
Lin, P., Liu, P.L.-F., 1998a. A numerical study of breaking waves in the surf zone. J. Fluid Mech. 359, 239–264.
Lin, P., Liu, P.L.-F., 1998b. Turbulence transport, vorticity dynamics, and solute mixing under plunging breaking waves in surf zone. J. Geophys. Res. 103 (C8), 15677–15694.
Lin, P., Chang, K.-A., Liu, P.L.-F., 1999. Runup and run-down of solitary waves on sloping beaches. J. Waterw. Port Coast. Ocean Eng. 125 (5), 247–255.
Lin, C., Ho, T.C., Chang, S.C., Hsieh, S.C., Chang, K.A., 2005. Vortex shedding induced by a solitary wave propagating over a submerged vertical plate. Int. J. Heat Fluid Flow 26, 894–904.
Liu, P.L.-F., Al-banaa, K., 2004. Solitary wave runup and force on a vertical barrier. J. Fluid Mech. 505, 225–233.
Liu, P.L.-F., Cheng, Y., 2001. A numerical study of the evolution of a solitary wave over a shelf. Phys. Fluids 13 (6), 1660–1667.
Liu, P.L.-F., Synolakis, C.E., Yeh, H., 1991. Report on the international workshop on long-wave run-up. J. Fluid Mech. 229, 675–688.
Losada, M.A., Vidal, C., Medina, R., 1989. Experimental study of the evolution of a solitary wave at an abrupt junction. J. Geophys. Res 94 (C10), 14557–14566.
Losada, I.J., Lara, J.L., Guanche, R., Gonzalez-Ondina, J.M., 2008. Numerical analysis of wave overtopping of rubble mound breakwaters. Coast. Eng. 55, 47–62.
Lynett, P.J., Liu, P.L.-F., Losada, I.J., Vidal, C., 2001. Solitary wave interaction with porous breakwaters. J. Waterw. Port Coast. Ocean Eng. 126 (6), 314–322.
Nakamura, T., Kuramitsu, Y., Mizutani, N., 2008. Tsunami scour around a square structure. Coastal Eng. J. 50 (2), 209–246.
Ramsden, J.D., 1996. Forces on a vertical wall due to long waves, bores, and dry-bed surges. J. Waterw. Port Coast. Ocean Eng. 122 (3), 134–141.

Stansby, P.K., 2003. Solitary wave runup and overtopping by a semi-implicit finite-volume shallow-water Boussinesq model. J. Hydraul. Res. 41 (6), 639–647.
Synolakis, C.E., Bernard, E.N., 2006. Tsunami science before and beyond boxing day 2004. Philos. Trans. R. Soc. A 364, 2231–2265.
Tonkin, S., Yeh, H., Kato, F., Sato, S., 2003. Tsunami scour around a cylinder. J. Fluid Mech. 496, 165–192.
Torres-Freyermuth, A., Losada, I.J., Lara, J.L., 2007. Modeling of surf zone processes on a natural beach using Reynolds-Averaged Navier–Stokes equations. J. Geophys. Res. 112, C09014. doi:10.1029/2006JC004050.
Xiao, H., Huang, W., 2008. Numerical modeling of wave runup and forces on an idealized beachfront house. Ocean Eng. 35, 106–116.
Yamamoto, Y., Takanashi, H., Hettiarachchi, S., Samarawickrama, S., 2006. Verification of the destruction mechanism of structures in Sri Lanka and Thailand due to the Indian ocean tsunami. Coastal Eng. J. 48 (2), 117–145.
Yeh, H., 2007. Design tsunami forces for onshore structures. J. Disaster Res. 2 (6), 531–536.
Yim, S.C., Yuk, D., Panizzo, A., Risio, M.D., Liu, P.L.-F., 2008. Numerical simulations of wave generation by a vertical plunger using RANS and SPH models. J. Waterw. Port Coast. Ocean Eng. 134 (3), 143–159.
Zhang, Q., Liu, P.L.-F., 2008. A numerical study of swash flows generated by bores. Coast. Eng. 55 (12), 1113–1134.